ACS APPLIED MATERIALS & INTERFACES

Research Article

www.acsami.org

Cell-Shaping Micropatterns for Quantitative Super-Resolution Microscopy Imaging of Membrane Mechanosensing Proteins

Anthony Fernandez,[†] Markville Bautista,[‡] Ramunas Stanciauskas,[†] Taerin Chung,[†] and Fabien Pinaud*[,†,‡,§]

[†]Department of Biological Sciences, [‡]Department of Chemistry, and [§]Department of Physics and Astronomy, University of Southern California, Los Angeles, California 90089, United States

Supporting Information

ABSTRACT: Patterning cells on microcontact-printed substrates is a powerful approach to control cell morphology and introduce specific mechanical cues on a cell's molecular organization. Although global changes in cellular architectures caused by micropatterns can easily be probed with diffraction-limited optical microscopy, studying molecular reorganizations at the nanoscale demands micropatterned substrates that accommodate the optical requirements of single molecule microscopy techniques. Here, we developed a simple micropatterning strategy that provides control of cellular architectures and is optimized for nanometer accuracy single molecule tracking and three-dimensional super-resolution imaging of plasma and nuclear membrane proteins in cells. This approach, based on fibronectin microcontact printing on hydrophobic organosilane monolayers, allows evanescent wave and light-sheet microscopy of cells whilst fulfilling the stringent optical demands of point reconstruction optical microscopy. By imposing steady-state mechanical cues on cells grown in these micropatterns, we reveal nanoscale remodeling in the dynamics and the structural organizations of the nuclear envelope mechanotransducing protein emerin and of the plasma membrane mechanosensing protein caveolin-1 using single particle tracking photoactivated localization microscopy and direct stochastic optical reconstruction microscopy imaging. In addition to allowing quantitative biophysical studies of mechanoresponsive membrane proteins, this approach provides an easy means to probe mechanical regulations in cellular membranes with high optical resolution and nanometer precision.

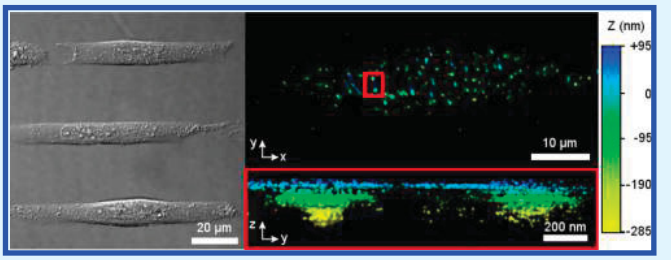

KEYWORDS: *cell micropatterning, self-assembled monolayer, super-resolution microscopy, single molecule tracking, membrane proteins, mechanosensing, nucleus, plasma membrane*

INTRODUCTION

Soft lithography and hard photolithography techniques are commonly used to investigate the adaptations that cells undertake when confronted with specific adhesion and mechanical cues.[1,2] Over the years, many approaches have been developed to control the adhesion of cultured cells and to micropattern them on a variety of substrates. For instance, surfaces functionalized with PEG can be used to physically print cells in predefined and fully customizable patterns[3] with a printing resolution of about 300 μm. Hydrogels have also been employed as three-dimensional (3D) substrates to pattern cell adhesion ligands and control cell distributions.[4,5] Other techniques, such as polydimethylsiloxane (PDMS) microstencils, avoid the complexities of developing specific surface chemistries or polymeric gels by allowing cells to attach directly to glass, in-between predesigned stencils.[6] In addition to these approaches, microstamping on coverslips spin-coated with polydimethylsiloxane (PDMS) and UV-etching of PEG-functionalized substrates are often employed to control the spatial immobilization of extracellular matrix proteins and induce cell adhesion in micron-size micropatterns.[7−10] These micropatterning techniques have been exploited to study the geometry-dependent mechanical responses of cells,[11−14] the dynamics of membrane pits as a function of cell spreading area,[15] or the spatial coordination between cell and nuclear shape.[16,17]

Because they are optically clear, micropatterning substrates are generally well suited for diffraction-limited optical imaging of cells by classical confocal microscopy, which provides imaging resolutions of approximately 200−250 nm, or by structured illumination microscopy, where optical resolutions can be pushed to 110 nm.[18,19] However, they are not always suited for nanometer precision imaging by single molecule super-resolution microscopy, which requires high photon counts, minimal background interference, and good optical coupling with high numerical aperture and short working distance objectives. For instance, spin-coating coverslips with pure PDMS[20] or using hydrogels[4,5] results in micron-thick polymer layers that impede high contrast evanescent wave excitation for single biomolecule imaging by total internal

Received: July 6, 2017
Accepted: August 2, 2017
Published: August 2, 2017

DOI: 10.1021/acsami.7b09743
ACS Appl. Mater. Interfaces XXXX, XXX, XXX−XXX

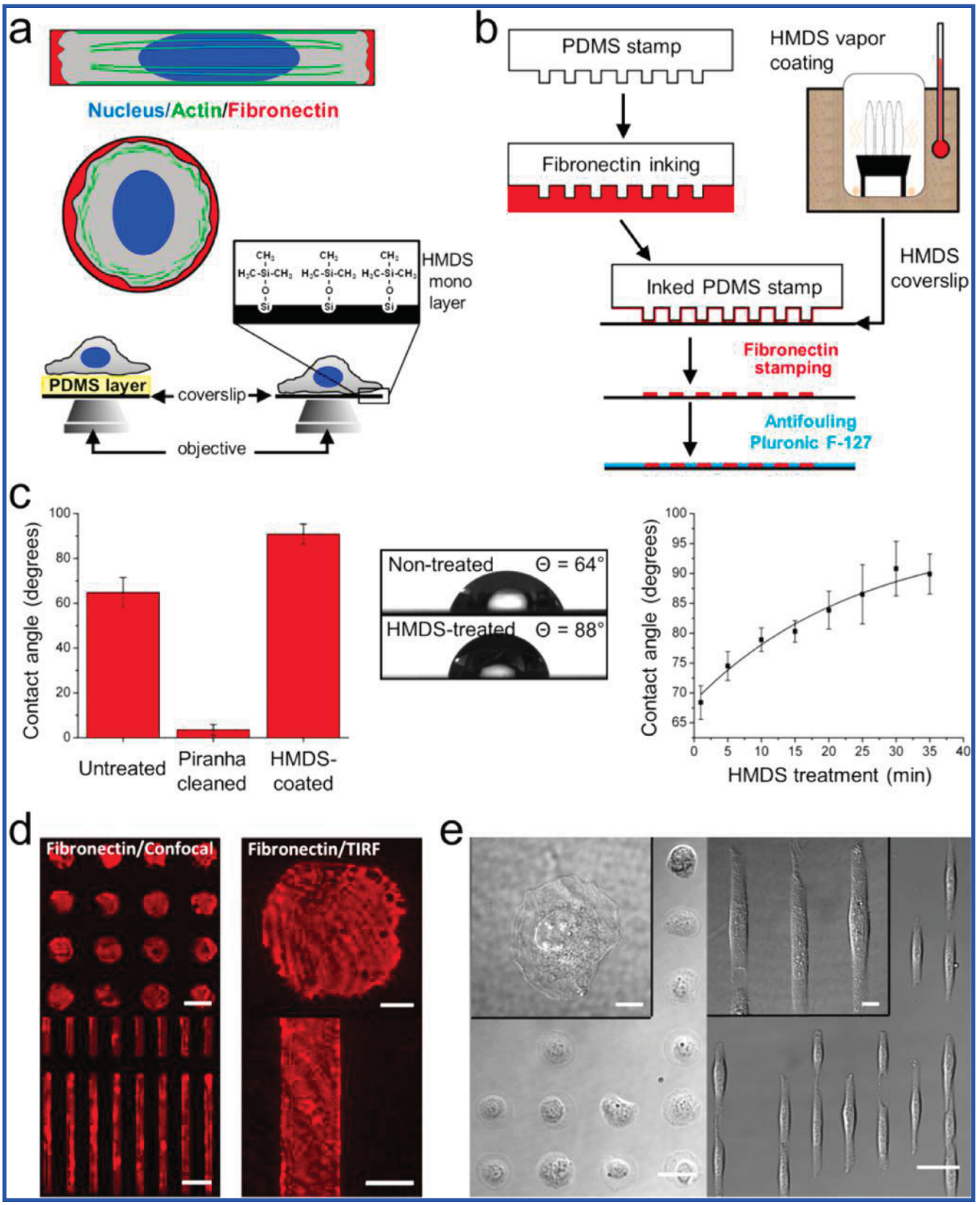

Figure 1. Cell micropatterning on HMDS-treated and fibronectin-functionalized coverslips. (a) Schematics of rectangular and circular micropatterned cells and substrate thickness comparison of PDMS-coated and HMDS-treated coverslips for cell microscopy imaging. (b) Fibronectin microstamping and functionalization of HMDS-treated coverslips with antifouling Pluronic F-127. (c) Comparison of water-surface contact angles (Θ) for untreated, Piranha-cleaned, and HMDS-treated coverslips (left), sessile drop images of water on nontreated and HMDS-treated glass (middle), and kinetics of HMDS monolayer deposition by vapor coating of coverslips (right). (d) Confocal and TIRF images of fluorescently labeled fibronectin after microstamping. Scale bars: 50 μm (left) and 10 μm (right). (e) Differential interference contrast images of micropatterned cells grown on HMDS-treated coverslips stamped with circular and rectangular fibronectin islands. Scale bars: 50 μm; insets: 10 μm.

DOI: 10.1021/acsami.7b09743
ACS Appl. Mater. Interfaces XXXX, XXX, XXX−XXX

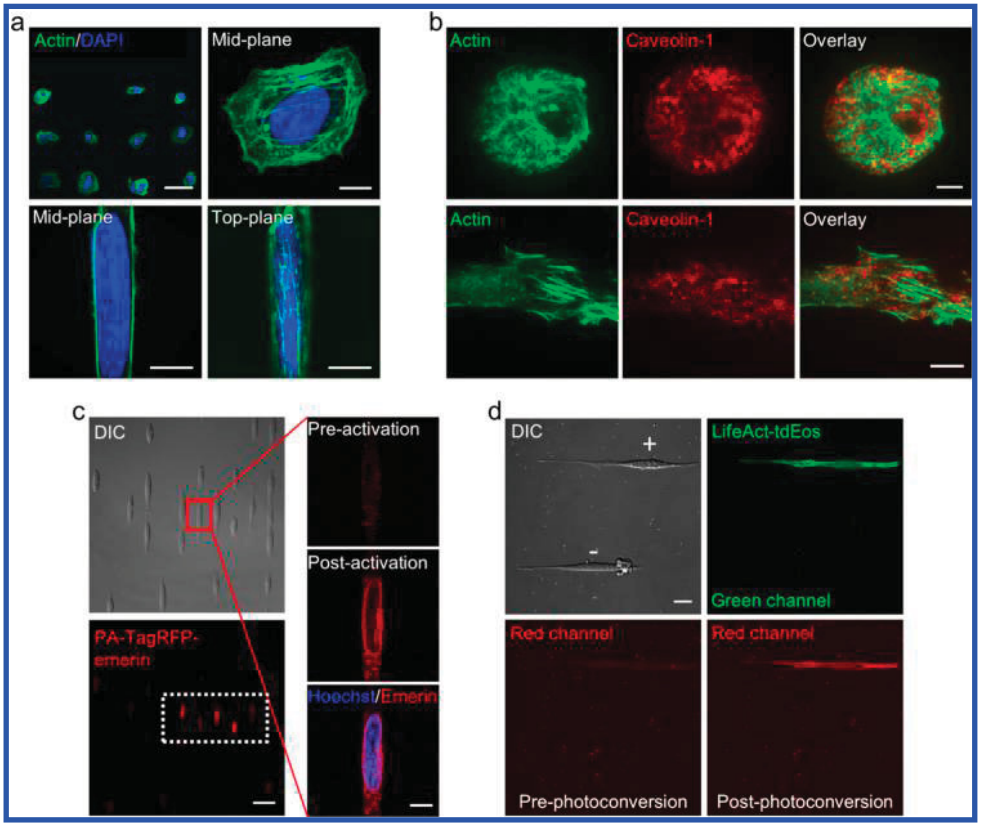

Figure 2. Fluorescence confocal and TIRF microscopy of cells micropatterned on HMDS coverslips. (a) Confocal microscopy images of fixed cells grown on circular and rectangular micropatterns and stained for actin and the nucleus. Scale bars: 50 μm (top left) and 10 μm. (b) TIRF microscopy images at the plasma membrane of fixed cells stained for actin and caveolin-1. Scale bars: 8 μm. (c) Confocal microscopy images and selective photoactivation of PA-TagRFP−emerin at the nuclear envelope of live cells. The delineated region of interest (ROI) (white) was photoactivated by confocal scanning with a 405 nm laser. Scale bars: 50 and 10 μm (zoom). (d) Confocal images and photoconversion of actin in live micropatterned cells transiently transfected with LifeAct−tandem dimer EOS (LifeAct−tdEos). The + and − signs correspond to a transfected and a nontransfected cell, respectively. Green to red photoconversion of LifeAct−tdEos was done over the entire field of view using a 405 nm laser excitation. Scale bar: 20 μm.

reflection fluorescence (TIRF) microscopy. In addition, fluorescent impurities and optical aberrations caused by the refractive index mismatch with such polymeric substrates[21] can rapidly degrade localization precision and resolution in point localization and reconstruction cellular imaging. Although direct physical printing of cells or UV-etching of micropatterns on thin pegylated substrates can offset these issues,[22] a drawback of these approaches is their requirements of expensive equipment and regular access to clean rooms, which makes them less convenient and cost-effective than microstamping techniques for biologists.

Here, we developed a simple microcontact printing approach on high tolerance coverslips to modulate cell shapes in micron-size patterns and image the dynamics and molecular organization of cellular nanostructures with a localization precision of 7−20 nm by single molecule TIRF and highly inclined and laminated optical sheet (HILO) microscopy. As cells squeezed into adhesion micropatterns that were smaller than their size, modifications of their mechanical landscape were probed by imaging changes in the nanoscale distribution of the mechanosensing proteins caveolin-1 (Cav1) and emerin at the plasma membrane and the nuclear envelope, respectively. Cav1 is a scaffolding membrane protein that oligomerizes into 80−100 nm caveolae invaginations and flat caveolin-1 scaffolds at the cell plasma membrane.[23,24] Caveolae display various shapes, from nearly flat structures to deep invaginations,[25,26] and act as membrane reservoirs whose assembly/disassembly cycles enable cells to adapt to mechanical strains and to changes in plasma membrane tensions.[27−29] Cav1 has been implicated in numerous pathologies that involve alterations in the mechanical properties of cells, including cell invasion[30] and defects in vascular contractility.[31,32] Emerin is a transmembrane protein of the inner nuclear envelope[33,34] that interacts with the nuclear lamina meshwork and the linker of nucleoskeleton and cytoskeleton (LINC) complex to mediate mechanical anchoring between the nucleoskeleton and the cytoskeleton.[35,36] Although its precise molecular distribution at the nuclear membrane is undefined, emerin participates in remodeling of perinuclear actin in response to force,[37−39] and is involved in mechanotransduction, maintenance of nuclear shape, and nucleus stiffening to resist applied tensions.[39−41] Emerin mutations lead to nuclear shape abnormalities[41] and nuclear envelope laminopathies[42] due to altered nuclear mechanics.

In this report, we combined cell micropatterning on thin microstamped substrates and single molecule super-resolution microscopy to impose and image steady-state changes in the mechanical landscape of cells. We show that the cellular mechanosensing functions of both Cav1 and emerin are coupled to their clustering state and their nanoscale distributions within the plasma and the nuclear membranes.

DOI: 10.1021/acsami.7b09743
ACS Appl. Mater. Interfaces XXXX, XXX, XXX−XXX

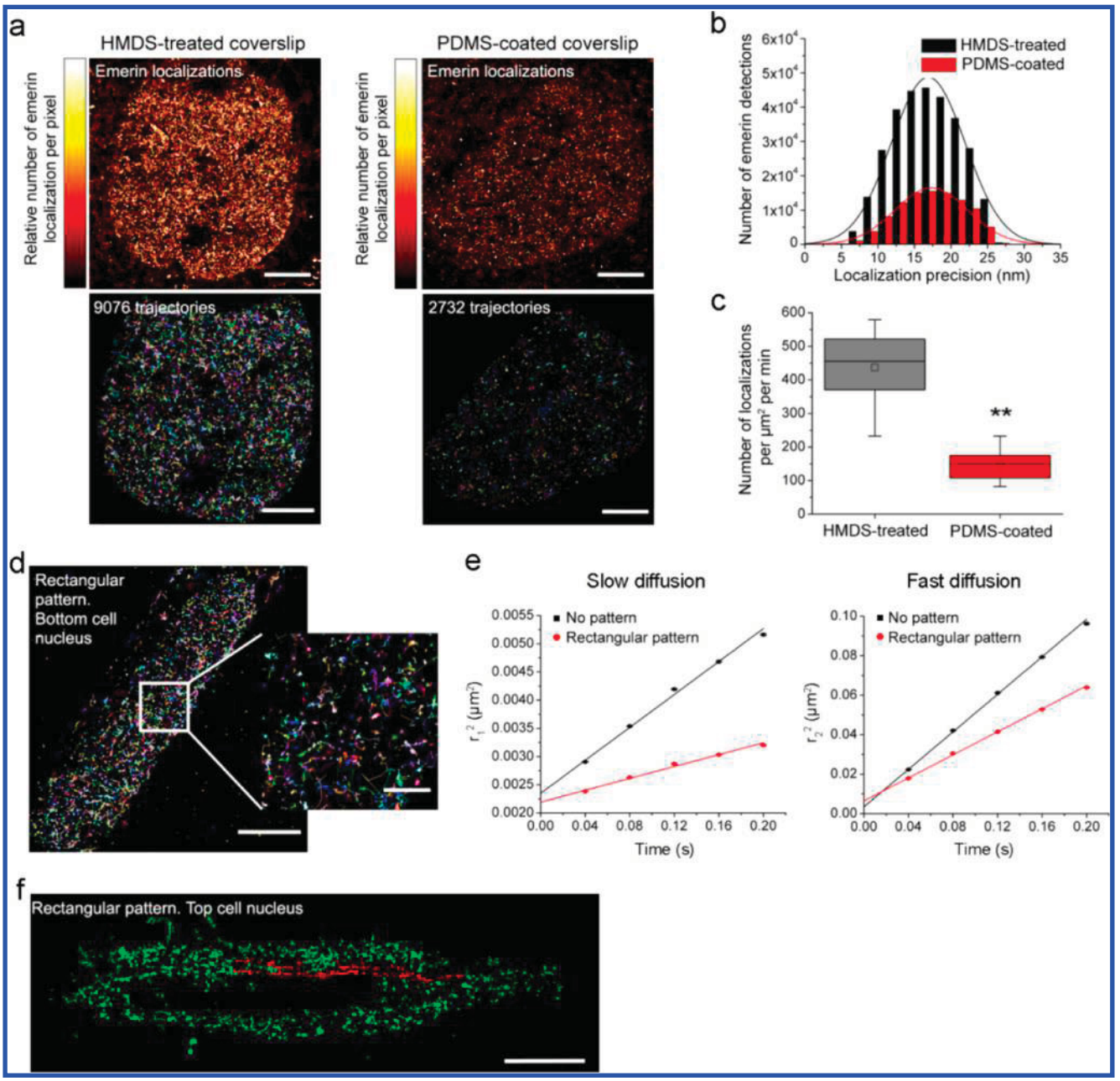

Figure 3. Single molecule tracking of emerin at the nuclear envelope of micropatterned cells. (a) Localization (top) and diffusion trajectories (bottom) of individual PA-TagRFP−emerins at the bottom nuclear membrane of live cells randomly grown on HMDS-treated (left) or PDMS-coated coverslips (right). Scale bars: 5 μm. (b) Localization precision of emerin in cells grown on HMDS-treated or PDMS-coated coverslips. (c) Detection efficiency of individual PA-TagRFP−emerins in cells imaged on HMDS- or PDMS-coated coverslips. The central squares and bars represent the mean of the distribution and its median, respectively. The box length represents the interquartile range, and the error bars are the standard deviation of the mean (**: *T*-test, $P < 0.01$). (d) Diffusion trajectories of emerin at the bottom nuclear membrane of a deformed nucleus for a cell grown on a 210 × 10 μm^2 micropattern. Scale bars: 10 and 2 μm (zoom). (e) Diffusion coefficient analysis by probability distribution of the squared displacement (PDSD) for the slow (left) and fast (right) diffusive behaviors of emerin at the bottom nuclear membrane of nonpatterned (black) and rectangular-patterned cells (red). Error bars represent the standard error of each mean at each time lag. (f) Diffusion trajectories of emerin at the top nuclear membrane of a deformed nucleus for a cell grown on a 210 × 10 μm^2 micropattern. Some trajectories have been highlighted in red to show their distribution along thin linear structures reminiscent of apical actin fibers. Scale bar: 5 μm.

RESULTS AND DISCUSSION

Functionalization of Coverslips and Cell Micropatterning. As an alternative to the micron-thick layers of spin-coated polymers generally employed for cell microstamping, we sought to develop a monolayer deposition chemistry with a monoreactive silane to generate glass coverslips where micropatterned cells could be imaged by single molecule microscopy with minimal optical interference (Figure 1a). Hexamethyldisilazane (HMDS), which forms a single siloxane bond with the silanol groups on glass coverslips, was deposited as a monolayer by vapor coating to make the coverslips hydrophobic[43] and to prime the glass surface for fibronectin microstamping and for site-blocking with antifouling agents (Figure 1b). Batches of coverslips were first cleaned and activated with a Piranha solution before being exposed to

DOI: 10.1021/acsami.7b09743
ACS Appl. Mater. Interfaces XXXX, XXX, XXX−XXX

HMDS vapor for 30 min, an incubation time sufficient to attain complete and homogenous monolayer deposition (Figure 1c). As confirmed by sessile drop goniometry, the HMDS-treated coverslips were significantly more hydrophobic than the nontreated coverslips with water-surface contact angles shifting from 65 to 88° after silanization (Figure 1c). The HMDS-treated coverslips remained hydrophobic, without showing any change in contact angle, for more than 1 week when stored under a dry atmosphere.

Direct micropatterning of fibronectin on the silanized coverslips was achieved by microcontact printing using 52 μm circular and 210 × 10 μm^2 rectangular PDMS stamps (Figure S1). Nonpatterned areas were then blocked with Pluronic F-127, a nontoxic, nonionic, and amphiphilic triblock copolymer composed of a hydrophobic poly(propylene glycol) domain that interacts with HMDS and two poly(ethylene glycol) domains that confer antifouling properties and prevent cell adhesion (Figure 1b). The stamping process was robust and fibronectin remained firmly and specifically attached on the coverslips after washing off excess Pluronic F-127 with phosphate-buffered saline (PBS). Confocal and TIRF microscopy of fibronectin after fluorescent staining revealed the effective formation of micropatterns with dimensions matching those of the applied stamps (Figure 1d). In comparison, TIRF imaging of fibronectin stamped on PDMS-coated coverslips was not possible because, even under optimized spin-coating conditions,[20] the resulting 5 μm thickness of the deposited polymer prevented an effective excitation of the stamped surfaces by the short-range TIRF evanescent field (Figures S2 and S3).

Cells seeded on the micropatterned coverslips adhered specifically to the fibronectin islands within 1 h of incubation and fully spread over the stamped areas after 4−6 h, adapting their overall shape to the dimensions of the patterns (Figure 1e). Pluronic F-127 effectively restricted cell adhesion and spreading outside the stamped regions, and cells could be continuously grown for 72 h within the micropatterns by alternating the use of serum-free cell media and daily 1−2 h feeding with 10% serum.

Fluorescence Microscopy Imaging of Micropatterned Cells. Fluorescently labeled cells were then imaged by confocal and TIRF microscopy to assess whether changes in cell morphology imposed by our thin adhesive micropatterns induced cytoskeletal reorganization and modification of the nuclear shapes similar to that observed for cells patterned on PDMS-coated coverslips.[16] After chemical fixation, cells micropatterned on HMDS-treated coverslips were dually labeled with phalloidin-iFluor 488 and the nuclear stain 4′,6-diamidino-2-phenylindole (DAPI), and were imaged by confocal scanning microscopy. Circular-shaped cells displayed "ring-like" distributions of F-actin bundles and a rounded nucleus, whereas rectangular-shaped cells had apical actin stress fibers that arched over and projected on either side of the nucleus deformed along the major cell axis, as previously reported[16,44] (Figure 2a and Video S1). Imaging cells patterned on PDMS-coated coverslips using TIRF microscopy was not possible because the polymer layer was too thick to allow evanescent wave excitation of the cell basal plasma membrane. Cells micropatterned on HMDS-treated glass, however, could be easily imaged by multicolor TIRF microscopy. TIRF excitation of cells costained with phalloidin-iFluor 488 and fluorescent antibodies against the membrane protein Cav1 provided high contrast imaging of the submembranous cortical actin and of cell surface caveolae invaginations, confirming the selective illumination of the plasma membrane (Figure 2b).

Cells micropatterned on HMDS coverslips could also be imaged with fluorescent probes optimized for single molecule and super-resolution microscopy, such as photoactivatable and photoconvertible fluorescent proteins. In live cells stably expressing the nuclear membrane protein emerin fused to PA-TagRFP, the expected nuclear envelope localization of the proteins was observed following photoactivation with 405 nm laser excitation (Figure 2c). Similarly, efficient photoconversion of fluorescently labeled actin was achieved for live cells transiently transfected with cDNA coding for the actin binding peptide LifeAct fused to tdEos (Figure 2d). At the coverslip surface, the presence of Pluronic F-127 did not affect cDNA transfection efficacies and the number of transfected cells was similar for micropatterned and nonmicropatterned cells.

Single Molecule Imaging and Tracking by Light-Sheet Microscopy in Live Cells. To assess the advantages of this silanization surface chemistry for single molecule detection in cells, we imaged the nanoscale diffusion of individual PA-TagRFP−emerin fusions at the nuclear envelope by single particle tracking photoactivated localization microscopy (sptPALM)[45] using HILO excitation.[46] For nonpatterned cells grown on HMDS glass functionalized with fibronectin, a shallow illumination angle of the HILO 405 nm activation and 561 nm imaging laser beams was sufficient to continuously photoactivate single emerin proteins and image their diffusion at the bottom nuclear envelope (Figure 3a and Video S2). For cells grown on thicker PDMS-coated glass, however, a steeper HILO illumination angle was required to achieve photoactivation and excitation of the nuclear envelope high above the coverslip surface (Figure 3a and Video S2). Although there was no significant difference in the localization precision of individual photoactivated emerins between both types of coverslips (Figure 3b), the number of single molecule detections per unit time was significantly lower on PDMS surfaces than on HMDS surfaces (Figure 3c). This lower detection efficiency on PDMS-coated coverslips can be attributed to the increased thickness of the laminated optical sheets and to the wavelength-dependent spatial mismatch between the 405 nm activating and the 561 nm imaging HILO beams at steep excitation angles, which resulted in a reduced photoactivation efficacy of PA-TagRFP−emerin at the imaging focal plane. Comparatively, on HMDS-treated surfaces, better optical coupling between the HILO beams and cells permitted a 3-fold higher density mapping of single emerin diffusion trajectories (Figure 3a).

To validate our sptPALM measurements on HMDS coverslips, we compared the diffusion properties of emerin determined by single particle tracking with that obtained by fluorescence recovery after photobleaching (FRAP) (Supporting Information). In ensemble FRAP analyses, fast (D_{fast} = 0.85 × 10^{-1} ± 0.1 × 10^{-1} μm^2/s, 19%) and slow (D_{slow} = 3.3 × 10^{-3} ± 0.1 × 10^{-3} μm^2/s, 81%) diffusive behaviors of emerin were observed at the bottom nuclear membrane, which were in good agreement with previously reported diffusion values of emerin and the presence of a nearly immobile fraction of this protein at the nuclear envelope (Figure S4).[33,47] For individual emerins, diffusion trajectories were obtained by two-dimensional (2D) Gaussian fitting of their diffraction-limited point-spread function and by linking the localized position of each molecule from frame to frame. Diffusion coefficients were determined using a two-parameter fit of the probability distribution of the

DOI: 10.1021/acsami.7b09743
ACS Appl. Mater. Interfaces XXXX, XXX, XXX−XXX

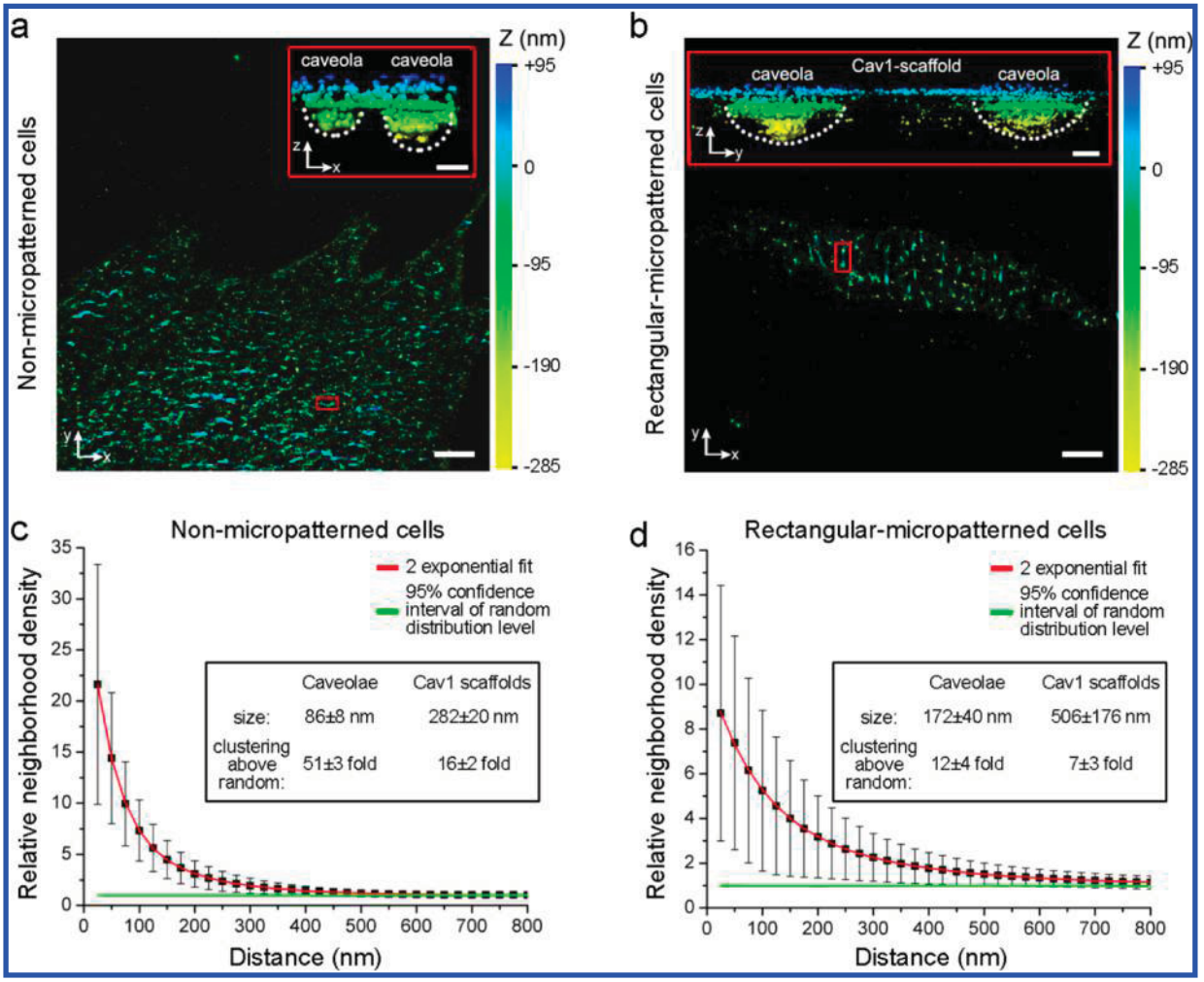

Figure 4. Super-resolution imaging and cluster analyses of plasma membrane caveolin-1 in cells. (a) Two-dimensional projection image of 3D Cav1 localizations at the membrane of a nonmicropatterned cell. Scale bar: 5 μm. Inset: *z*, *x* rendering of two super-resolved caveolae in a region of interest (red). Scale bar: 100 nm. (b) Two-dimensional projection image of 3D Cav1 localizations in a MEF cell grown on a 210 × 10 μm^2 fibronectin micropattern. Scale bar: 5 μm. Inset: *z*, *y* rendering showing the enlargement and the increased invagination of caveolae and the presence of flatter Cav1 membrane scaffolds in a region of interest (red). Scale bar: 100 nm. (c) Cluster analysis of membrane Cav1 in nonpatterned cells. The neighborhood density is best fit by two exponentials (red), revealing the high clustering of Cav1 into small caveolae and its lesser clustering into larger Cav1 scaffolds at the plasma membrane (inset). (d) Cluster analysis of Cav1 in 210 × 10 μm^2 rectangular-patterned cells. Both caveolae and Cav1 scaffolds increase in size at the plasma membrane of micropatterned cells (inset).

squared displacements (PDSD)[48] to account for the fast and slow diffusions observed by FRAP. This analysis revealed that most emerin (78%) diffused slowly at the bottom nuclear envelope (D_{slow} = 3.65 × 10^{-3} ± 0.14 × 10^{-3} μm^2/s), and a smaller population (22%) diffused more rapidly (D_{fast} = 1.19 × 10^{-1} ± 0.02 × 10^{-1} μm^2/s), which is in good agreement with the ensemble FRAP data (Figure 3e).

Interestingly, when the same single molecule tracking and diffusion analyses were performed in cells grown on rectangular fibronectin islands, both the fast and slow diffusion coefficients of emerin in deformed nuclei were reduced by about 2-fold (D_{slow} = 1.32 × 10^{-3} ± 0.1 × 10^{-3} μm^2/s, 85%; and D_{fast} = 0.73 × 10^{-1} ± 0.02 × 10^{-1} μm^2/s, 15%; Figure 3d,e). At the top nuclear membrane of these micropatterned cells, many emerin trajectories also distributed along thin linear structures reminiscent of the apical actin fibers projecting above elongated nuclei (Figure 3f). Both observations are consistent with the expected mechanosensing role of emerin at the nuclear envelope[39,41,49] and its proposed ability to reinforce interactions between actin, the LINC complex, and the nuclear lamin meshwork to maintain the stiffness of the nucleus when it is mechanically stressed or compressed.[50] Indeed, direct binding of emerin to nuclear lamin reduces its diffusion at the nuclear membrane[51] and compressive forces from apical actin fibers on deformed nuclei induce the alignment of lamin and LINC complex proteins along actin cables.[19] The observed slower membrane diffusion of emerin and its distribution along actin-like fibers imply an increased interaction of emerin with the nuclear lamin meshwork and the LINC complex in deformed nuclei compared to normal nuclei. Importantly, these data also demonstrate that micropatterning of cells on HMDS-treated coverslips effectively induces nuclear mechanical strains and dynamic responses from mechanosensing proteins that can easily be probed by ultrahigh precision imaging with single molecule sensitivity.

Super-Resolution Microscopy of Membrane Mechanosensing Proteins in Micropatterned Cells. We then assessed the suitability of our micropatterning chemistry for super-resolution microscopy imaging. Using the plasma membrane mechanosensing protein Cav1 as a first model, we

DOI: 10.1021/acsami.7b09743
ACS Appl. Mater. Interfaces XXXX, XXX, XXX−XXX

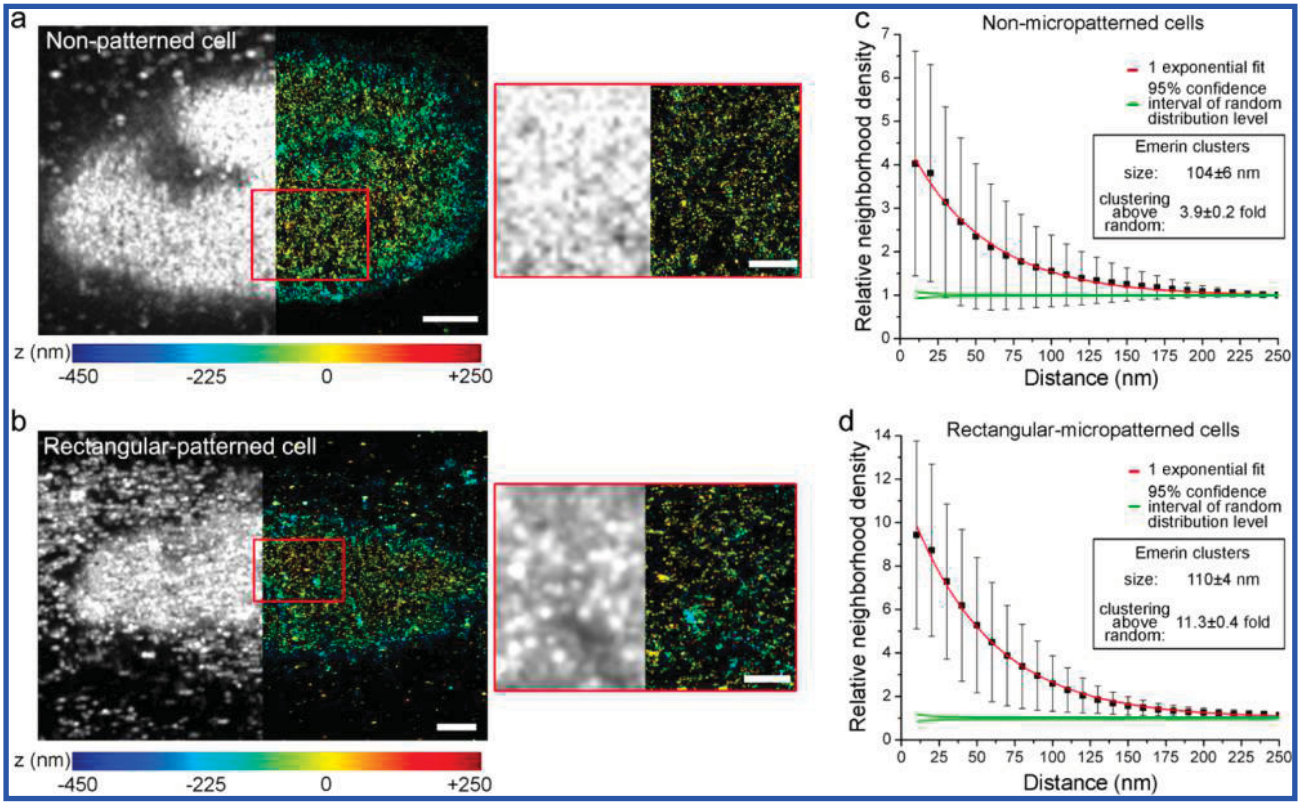

Figure 5. Super-resolution imaging and cluster analyses of nuclear membrane emerin in cells. (a) HILO imaging (left half) and 3D-dSTORM reconstruction (right half) of SNAP−emerin at the bottom nuclear membrane of a nonpatterned cell. Emerin clusters from a region of interest (red) are shown in more detail on the right. Scale bars: 2 μm (left) and 1 μm (right). (b) HILO imaging (left half) and 3D-dSTORM reconstruction (right half) of emerin at the bottom nuclear membrane of a cell grown on a 210 × 10 μm^2 fibronectin micropattern. Emerin clusters from a region of interest (red) are shown in more detail on the right. Scale bars: 3 μm (left) and 1 μm. (c) Cluster analysis of emerin in normal nuclei for nonpatterned cells. The neighborhood density is best fit by a single exponential (red), revealing the clustering of emerin into nanodomains 104 ± 6 nm in size and at a density 4-fold above that expected for a random distribution (inset). (d) Cluster analysis of emerin in deformed nuclei for cells grown on 210 × 10 μm^2 rectangular micropatterns. The size of emerin clusters is similar to that of nonpatterned cells (110 ± 4 nm), but the clustering density increases 11-fold above that expected for a random nuclear membrane distribution (inset).

performed three-dimensional direct stochastic optical reconstruction microscopy (3D-dSTORM)[52] to resolve and quantify the nanoscale organization of Cav1 assemblies at the basal surface of cells. Mouse embryonic fibroblasts (MEFs) derived from Cav1 knockout mice[53] and rescued by the stable expression of Cav1 fused to a SNAP tag[54] were fixed and labeled with the fluorescent dye BG-A647 before 3D-dSTORM imaging in photoswitching buffers. For rectangular-shaped cells on HMDS coverslips and nonpatterned cells grown on fibronectin-coated glass, individual Cav1 at the cell plasma membrane could be imaged by TIRF and localized with an accuracy of 7, 9, and 14 nm in the *x*, *y*, and *z* dimensions, respectively (Figure S5 and Video S3). In comparison, Cav1 at the membrane of cells grown on thicker PDMS-coated coverslips could only be imaged by HILO, which resulted in a significantly reduced localization accuracy in all three dimensions (14, 13, and 109 nm in *x*, *y*, and *z*) due to out-of-focus background fluorescence interference from submembranous Cav1 pools (Figure S5 and Video S3). In super-resolved and three-dimensional renderings of Cav1 localizations at the plasma membrane of cells, membrane-lined invaginations bulging toward the cytoplasm were detected together with flatter Cav1-rich membrane domains (Figure 4a,b). Spatial distribution analyses of the clustered point patterns formed by Cav1 at the membrane of nonmicropatterned cells revealed the coexistence of two types of Cav1 nanoassemblies that were 51 ± 3-fold and 16 ± 2-fold more clustered than that expected for a completely random distribution of Cav1 (Figure 4c). The typical clustering lengths of these two types of Cav1 clusters were 86 ± 8 and 282 ± 20 nm, respectively (Figure 4c), which is in good agreement with the expected 80−100 nm size of caveolae invaginations and that of the recently described Cav1 membrane scaffolds.[55] Similar cluster analyses on rectangular micropatterned cells indicated that both caveolae and Cav1 scaffolds were significantly larger, with sizes of 172 ± 40 and 506 ± 176 nm, respectively (Figure 4d). These modifications in Cav1 cluster organization likely reflect a remodeling of the plasma membrane and changes in cell adhesion/tension properties as cells adapt to the narrow rectangular micropatterns, notably via cytoskeletal actin reorganizations and depletion of basal actin stress fibers[56] (Figure 2 and Video 1). In particular, the apparent enlargement of caveolae and their extended invagination (Figure 4b) are consistent with an increased abundance of multilobed caveolae clusters, such as caveolar rosettes, which generally correlates with the absence or the reduced formation of actin stress fibers.[29] Consistent with the mechanosensitive functions of Cav1 and its clustering plasticity in response to variations in membrane tensions,[27,57] these data indicate that changes in cell shape on fibronectin micropatterns effectively result in mechanical strains in the bottom cell plasma membrane, which induce significant spatial reorganizations of caveolae and Cav1 scaffolds at the nanoscale.

DOI: 10.1021/acsami.7b09743
ACS Appl. Mater. Interfaces XXXX, XXX, XXX−XXX

Using HILO 3D-dSTORM super-resolution imaging, we also studied the effects of nuclear deformation on the nanoscale spatial distribution of emerin at the bottom nuclear membrane of micropatterned cells. U2OS cells expressing a SNAP−emerin fusion were grown randomly on fibronectin-coated HMDS coverslips or micropatterned on 210 × 10 μm^2 rectangular fibronectin strips before fixation, BG-A647 staining, and imaging. Although the nuclear membrane distribution of emerin appeared homogenous in diffraction-limited confocal (Figure S4) and HILO images (Figure 5a,b), super-resolution 3D-dSTORM revealed that emerin is actually extensively clustered at the nuclear envelope of both patterned and nonpatterned cells (Figure 5a,b). In nonpatterned cells with a normal nuclear shape, emerin was 4-fold more clustered than expected for a completely random distribution of the protein at the nuclear membrane, and the typical size of emerin clusters was 104 ± 6 nm (Figure 5c). At the membrane of deformed nuclei in the rectangular micropatterned cells, the size of emerin clusters was unchanged (110 ± 4 nm), but emerin was 3-fold more clustered in these nanodomains than in normal nuclei, with an apparent clustering that was 11-fold higher than expected for a random distribution (Figure 5d). This indicates that mechanical strains imposed at the nuclear envelop by the rectangular micropatterns result in the spatial redistribution of emerin into denser nanoclusters and that its mechanosensing functions are coupled to its clustering state at the nuclear membrane. Such an increased clustering of emerin is consistent with its slower diffusion observed on deformed nuclear envelops and with its expected enhanced binding to LINC complex proteins and to the nuclear lamin network in mechanically stressed nuclei.[50]

CONCLUSIONS

We demonstrated that cells cultured in vitro can easily be micropatterned and imaged with nanometer precision on ultrathin glass substrates via simple vapor coating of hydrophobic silanes, microstamping of fibronectin, and surface blocking using Pluronic F-127 as a biofouling agent. Compared to microcontact printing on spin-coated and micron-thick elastomeric polymer substrates such as PDMS, monolayer coating with HMDS is less labor and time intensive, and, importantly, it improves optical coupling with micropatterned cells to provide optimal detection efficiencies for single molecule tracking and super-resolution microscopy. As such, our approach has advantages similar to deep UV photolithography on pegylated glass without the need for expensive quartz photomasks and the difficult optimization of the proximity gap between mask and glass. The robust and stable adhesion of extracellular matrix proteins and antifouling agents on HMDS coverslips allows the culture and transfection of individual cells with, potentially, any micropatterning geometries. In addition to facilitating fluorescence cell imaging with traditional probes and microscopy techniques, microstamping on HMDS-treated coverslips also allows high-resolution imaging of cellular membranes by evanescent wave and light-sheet excitation under steady-state mechanical strain.

By combining cell micropatterning and single molecule microscopy, we showed that mechanosensing membrane proteins could be quantitatively studied in cells subjected to specific mechanical cues, and with an imaging precision of a few nanometers, which is far beyond the optical diffraction limit. In particular, we established that Cav1 at the cell plasma membrane and emerin at the nuclear membrane undergo significant changes in dynamics and nanoscale structural organizations when the mechanical landscape of cells and their actin organization is modified upon adhesion and spreading on 10 μm wide patterns. We showed that Cav1 assembles into two distinct nanostructures at the plasma membrane, 3D-shaped caveolae and flatter Cav1 scaffolds, and that these assemblies increase in size when cells are forced to adhere on thin fibronectin strips. These structural reorganizations are consistent with the mechanosensing and tension-buffering role of Cav1 and the need to rebalance membrane tensions as the membrane area and cytoskeletal attachments are remodeled in adhesion micropatterns narrower than the size of the cells. We also demonstrated that emerin largely clusters into ∼100 nm nanodomains at the nuclear envelope of nonstrained nuclei, and that it redistributes into denser clusters and undergoes slower lateral diffusion at the membrane of mechanically stressed and deformed nuclei for micropatterned cells. This increased emerin clustering, which is reminiscent of the mechano-induced clustering of integrins for transmembrane force transmission at the cell surface,[58,59] might reflect a need to maintain the stiffness of compressed nuclei via reinforced lamin/LINC complex/actin linkages. Further studies of emerin nanoscale clustering as a function of nuclear deformation and of emerin mutants that induce laminopathies but localize correctly at the nuclear membrane could yield new insights into the normal mechanosensing functions of emerin and into the pathogenesis of Emery−Dreifuss dystrophy.

Overall, our micropatterning and imaging techniques open up new prospects to quantitatively study the molecular mechanobiology of cells with single molecule sensitivity and nanometer precision.

MATERIALS AND METHODS

PDMS Stamp Preparation. PDMS stamps with 30 × 30 circular or rectangular micropatterns were prepared from silicon masters produced by reactive ion etching using a chrome mask (soda lime substrate; Photo Sciences, Torrance, CA). The circular micropatterns are 52 μm in diameter with periodic intervals of 30 μm. The rectangular micropatterns are 210 × 10 μm^2 in size with the same periodic intervals of 30 μm. The depth of these silicon masters is 15 μm. After surface fluorosilanization of the masters with fluorosilane vapors (tridecafluoro-1,1,2,2-tetrahydrooctyl-1-trichlorosilane) for 90 min under vacuum, a degassed mixture of 40 g of PDMS (Sylgard 184) and 4 g of curing agent (Dow Corning, Midland, MI) was slowly poured into the silicon masters, and another degassing step was performed to avoid unwanted bubbles. After curing for 3 h at 65 °C and overnight at room temperature (RT), the PDMS stamps were removed slowly from the silicon master using a razor blade. PDMS stamps were routinely used for a period of 3−4 months without any loss in stamping efficacy.

HMDS Coating of Glass Coverslips, Fibronectin Microcontact Printing, and Cell Micropatterning. High precision microscope glass coverslips (Marienfeld, #1.5, Ø25 mm) were cleaned using a Piranha solution made of a 3:1 (v/v) mixture of 18 M sulfuric acid and 30% hydrogen peroxide for 5 min and rinsed thoroughly with deionized (DI) water. Following desiccation, the coverslips were heated to 80 °C for 30 min in a sealed glass jar containing 100 μL of hexamethyldisilazane (HMDS). After vapor coating, excess HMDS was evaporated and the coverslips were heated to 100 °C. HMDS-treated coverslips were stored in a separate and sealed glass container flushed with nitrogen. Sessile drop goniometry measurements were performed on a Tantec Contact Angle Meter by placing a small drop of water on five different HMDS-treated coverslips per condition and by taking 10 measurements per coverslip to generate average contact angle readings.

DOI: 10.1021/acsami.7b09743
ACS Appl. Mater. Interfaces XXXX, XXX, XXX−XXX

For fibronectin microcontact printing, PDMS stamps were coated with a 0.1 mg/mL fibronectin solution in PBS for 1 h. Stamps were then rinsed once with ethanol and briefly dried. Within 1 min after drying, an HMDS-treated coverslip was applied to the stamp with light pressure for 5 min. Upon removal, the coverslip was placed in a humid environment for 10 min, and then dried. Before cell plating, stamped coverslips were immersed for 10 min in a sterile filtered 1% solution of Pluronic F-127 (Sigma) in DI water and thoroughly rinsed in sterile PBS. To image the stamped fibronectin micropatterns, HMDS-treated and PDMS-coated coverslips stamped with fibronectin and functionalized with Pluronic F-127 were fluorescently stained for 1 h with a 3.25 μM solution of Cy3B-NHS (GE Healthcare Life Sciences) in PBS before washing in PBS and imaging by confocal or TIRF microscopy. After stamping, PDMS stamps were immersed in DI water for 30 min to remove residual fibronectin and salts, cleaned in an ultrasonic bath at 60 °C for 30 min, then immersed in 100% ethanol and cleaned for another 30 min at 60 °C in an ultrasonic bath before drying and storage.

Cells were maintained in Dulbecco's modified Eagle's medium (DMEM; Lonza) supplemented with 10% fetal bovine serum (FBS; Gibco) in a humidified incubator at 37 °C, supplied with 5% CO_2. Trypsinized cells resuspended in DMEM + 10% FBS were plated on fibronectin-stamped and Pluronic F-127-blocked coverslips and were allowed to attach for 6 h at 37 °C, after which the cell media was gently exchanged with serum-free DMEM. Micropatterned cells were maintained in serum-free DMEM at 37 °C and 10% serum was added for 1−2 h every 24 h.

Plasmids, Cell Lines, and Cell Labeling. For the expression of PA-TagRFP−emerin, a pEGFP-N1 plasmid backbone encoding emerin fused to the C-terminus of PA-TagRFP was produced by XbaI and KpnI insertion and polymerase chain reaction fusion of human emerin cDNA. A stable monoclonal U2OS cell line constitutively expressing PA-TagRFP−emerin was obtained after transfection with XtremeGene HP (Roche), selection with 100 μM of Geneticin (G418), and clonal isolation by serial dilution. For confocal imaging, live U2OS cells expressing PA-TagRFP−emerin and grown in micropatterns were further stained with 1:1000 Hoechst 33342 (Thermo) in Hank's balanced salt solution (HBSS) buffer (Corning), rinsed three times, and imaged in 37 °C HBSS. For single molecule tracking of emerin by sptPALM, no additional nuclear staining was performed.

For the expression of SNAP−emerin, emerin was fused to the C-terminus of a SNAP tag by inserting human emerin cDNA in a pSNAP-tag(m) plasmid (NEB) via AscI and XhoI restriction sites. U2OS cells grown in six-well plates were transiently transfected with this plasmid using XtremeGene HP, trypsinized 24 h after transfection, and seeded on micropatterned coverslips. Forty-eight hours post transfection, cells were fixed with 4% paraformaldehyde in PBS for 15 min, permeabilized with 0.1% Triton X-100 for 15 min, and blocked with 4% bovine serum albumin (BSA) + 0.1% Tween-20 for 30 min, all at RT. Cells were then stained with 1:1000 SNAP AlexaFluor 647 (BG-A647, NEB) in 4% BSA + 0.1% Tween-20 for 1 h at 37 °C, then thoroughly washed before super-resolution imaging.

For the expression of Cav1, a multiclonal cell line stably expressing Cav1−SNAP was generated after transfection of a pEGFP-N1 plasmid backbone encoding the sequence for canine Cav1 fused to the N-terminus of a SNAP tag in 3T3 MEF KO cells originating from Cav1 knockout mouse (ATCC CRL-2753). Cell imaging was performed after cell fixation and Cav1−SNAP staining with BG-A647 as previously described.

For actin imaging with the photoconvertible tandem dimer Eos fluorescent protein (tdEos), U2OS cells grown in micropatterns were transiently transfected with a pDendra2-N plasmid backbone encoding the LifeAct peptide fused to the N-terminus of tdEos (LifeAct−tdEos).

For actin and Cav1 immunostaining, U2OS cells were fixed as previously described. Actin was stained with 1:1000 CytoPainter phalloidin-iFluor 488 (Abcam), and Cav1 was detected with 1:1000 anti-Cav1 rabbit antibody (N-20, Santa Cruz Biotechnology) followed by a 1:1000 staining with Alexa-647 goat antirabbit antibody (Life Technologies). Coverslips were mounted using Fluormount G with DAPI (Hatfield, PA) to visualize the nuclei.

Confocal, TIRF, and HILO Microscopy. Confocal microscopy images were acquired on a Nikon C2 inverted confocal microscope equipped with a 20× 0.75 NA objective (Nikon) and a 60× 1.40 NA objective (Nikon), with laser lines (405, 488, 561, and 647 nm) and with appropriate dichroic mirrors and emission filters for imaging DAPI/Hoechst (483/32 nm, Semrock), iFluor 488 and tdEos (525/50 nm, Semrock), PA-TagRFP and photoconverted tdEos (600/50 nm, Chroma), and Alexa-647 (700/75 nm, Chroma).

TIRF and HILO microscopy images were acquired on an inverted Nikon Eclipse Ti-E microscope, equipped with a 100× 1.49 NA objective (Nikon), an iXon EMCCD camera (Andor), perfect focus drift compensation optics, an astigmatic lens for 3D super-resolution imaging, a piezo z-scanner for calibration of 3D super-resolution images (Mad City Labs), laser lines at 405, 488, 561, and 647 nm (Agilent), a multiband pass ZET405/488/561/647× excitation filter (Chroma), a quad-band ZT405/488/561/647 dichroic mirror (Chroma), and appropriate emission filters for sptPALM imaging of PA-TagRFP (600/50 nm, Chroma) and 3D-dSTORM imaging of Alexa-647 (700/75 nm, Chroma).

Single Particle Tracking and Diffusion Analyses. sptPALM of PA-TagRFP−emerin was performed in 37 °C HBSS buffer by HILO excitation of the bottom nuclear membrane of cells with continuous and low power photoactivation at 405 nm and excitation at 561 nm. The HILO illumination angle was θ = 51.6° for cells on HMDS coverslips and θ = 41.8° for cells on PDMS-coated coverslips. Images were acquired continuously for 1 min at a frame rate of 40 ms/frame. Single molecule localization and tracking were performed using SlimFast, a single particle detection and tracking software written in Matlab that uses multiple-target tracing algorithms[60] and was kindly provided by Christian Ritcher and Jacob Piehler. Localizations were done on thousands of individual molecules in multiple cells (n = 8) for each condition, by 2D Gaussian fitting of the point-spread function of each activated PA-TagRFP−emerin in each frame. Localization precisions were determined using the method of Thompson et al.[61] Diffusion trajectories were built by linking individual localized positions from one frame to the other, taking into account blinking statistics and local particle densities. Only trajectories with at least three step sizes were kept for diffusion analyses by probability distribution of square displacement (PDSD).[48] For the first five time lags t, each Pr^2 curve was fit with the general model

$$P(\vec{r}^2, t) = 1 - \sum_{i=1}^{n} \alpha_i(t)\, e^{-r^2/r_i^2(t)}$$

$$\sum_{i=1}^{n} \alpha_i(t) = 1 \quad (1)$$

where $r_i^2(t)$ and $\alpha_i(t)$ are the square displacement and the fraction corresponding to i numbers of diffusive behaviors at each time lag t. The Pr^2 distributions of PA-TagRFP−emerin were fit with i = 2 behaviors.

Error bars for each r_i^2 in $r_i^2(t)$ curves were determined using $\frac{r_i^2}{\sqrt{N}}$, where N is the number of data points used to build each probability distribution function. Diffusion coefficients were obtained by fitting $r_i^2(t)$ curves in Origin software (OriginLab) using a free Brownian diffusion model with localization error

$$r^2 = 4Dt + 4\sigma^2 \quad (2)$$

All of the diffusion coefficients D are reported in micrometer squared per second ± standard deviation of the fit value.

Three-Dimensional Super-Resolution Microscopy by dSTORM and Cluster Analyses. Three-dimensional dSTORM imaging of Cav1−SNAP and SNAP−emerin labeled with BG-A647 was done by TIRF (for Cav1) or HILO (for emerin or for Cav1 on PDMS-coated coated coverslips) using an astigmatic lens in the emission path. Z-calibration and sample drift corrections were performed using a few 40 nm TransFluoSphere beads (488/685 nm,

DOI: 10.1021/acsami.7b09743
ACS Appl. Mater. Interfaces XXXX, XXX, XXX−XXX

Life Technologies) as fiducials markers spread on the cell samples. A photoswitching buffer composed of 10% glucose, 0.5 mg/mL glucose oxidase (Sigma), 40 μg/mL catalase (Sigma), and 1% β-mercaptoethanol (Sigma) was used when driving A647 to the dark state and during subsequent continuous photoswitching with a low power 488 nm laser and imaging at 80 ms/frame with 647 nm laser excitation. Imaging was performed until the number of detected molecules on a cell was equivalent to background stochastic events outside the cell area, typically after ~10 000−15 000 frames. Single molecule localizations and z-position assignments were done using rapidSTORM (version 3.3.1),[62] sample drift and over-counting corrections for molecules appearing in consecutive frames were done using PALMsiever,[63] and 2D/3D renderings of super-resolved images were done using ImageJ[64] and USCF Chimera. Localization precisions (σ) in the x, y, and z dimensions were evaluated as previously described[65] using grouped point-clusters identified in consecutive frames, generating histograms of localizations by aligning centers of mass, and fitting the histograms with a Gaussian function (Figure S5).

The x and y coordinates of each single molecule corrected for drift and over-counting (grouping of consecutive localizations that fall within an error radius $(\sigma_x + \sigma_y)/2$ into a single averaged localization point, typically 5−7% of all detections) were imported in Microsoft Excel where regions of interest (ROIs) were selected for cluster analyses. ROIs were 10 μm × 10 μm in size for Cav1 (n = 16 ROIs, 7−9 cells) and 2 μm × 2 μm for emerin (n = 16 ROIs, 3−4 cells), and were typically chosen in plasma and nuclear membrane areas with homogenous z ranges and away from the membrane edges.

Protein clustering was determined by analysis with an edge-corrected neighborhood density function (NDF).[66−68] The NDF is a pairwise-correlation function similar to O-ring statistics, which tallies the density of detected proteins within a ring of outer radius r and width Δr located at a distance r from a protein position in the pattern and for all $r + \Delta r$ inside the pattern. The density of proteins as a function of distance from an average protein was obtained with

$$D_r = \frac{\sum N_r}{\sum A_r} \tag{3}$$

where N_r is the number of neighbors and A_r is the area summed over all proteins. For Cav1 ROIs, NDF analyses were done over an 800 nm distance with a fixed ring width of 25 nm and a ring radius increasing by 25 nm steps. For emerin ROIs, NDFs were done over a 600 nm distance with a fixed ring width of 10 nm and a ring radius increasing by 10 nm steps. To average NDF statistics from multiple ROIs in different cells and make them sample-size independent, D_r was further standardized by dividing it by the mean density of detected proteins across the entire ROI. Thus, an NDF value at a given radius indicates the relative protein clustering as compared to the average density across the entire sample. This relative NDF is also expected to give a value of 1 for a completely random spatial distribution of proteins. Ninety-five percent confidence intervals for complete spatial randomness were obtained by averaging Monte Carlo simulations of random protein distributions with area and number of Cav1 or emerin equal to that of each ROI (10 simulations per ROI for Cav1 and 60 simulations per ROI for emerin).

Considering that the probability density of proteins in two-dimensional clusters decays approximately as an exponential function,[69] the relative NDF curves averaged across multiple ROIs and multiple cells were fit using models derived from Veatch et al.[70]

$$\text{relative NDF} = \left\{A \exp\left(\frac{-r}{\varepsilon}\right) + 1\right\} * g(r)^{\text{PSF}} \tag{4}$$

for a single distribution of cluster length (e.g., emerin), or

$$\text{relative NDF} = \left\{A_1 \exp\left(\frac{-r}{\varepsilon_1}\right) + A_2 \exp\left(\frac{-r}{\varepsilon_2}\right) + 1\right\} * g(r)^{\text{PSF}} \tag{5}$$

for a distribution of cluster length that includes two populations (e.g., Cav1). Here, ε is the typical half-maximum cluster length, A is the average clustering factor, * denotes a two-dimensional convolution, and $g(r)^{\text{PSF}}$ is the correlation function of the effective point-spread function (PSF) of uncertainty in position determination for the dSTORM experiments. $g(r)^{\text{PSF}}$ corrects the NDF for contributions from multiple single molecule appearances (blinking) to the overall spatial distribution. Considering a Gaussian-shaped form of the PSF,[70] $g(r)^{\text{PSF}}$ was defined as

$$g(r)^{\text{PSF}} = \frac{1}{4\pi\sigma^2} \exp\left(\frac{-r^2}{4\sigma^2}\right) \tag{6}$$

where σ is the average uncertainty in position determination, assessed experimentally as described above.

We note that eqs 4 and 5 above do not include the density-dependent over-counting term of eq 1 in Veatch et al.,[70] because over-counting corrections were performed prior to building NDF curve distributions. The 1:1 SNAP/BG-A647 labeling use in our dSTORM experiments and the nature of NDF analyses also dampen the effect of apparent short-scale clustering within position uncertainty distances on the correlation function. After fitting relative NDF curves, the typical clustering lengths and clustering factors for Cav1 and emerin clusters are reported as $2\varepsilon \pm$ standard error of the fit and as $A \pm$ standard error of the fit, respectively.

■ ASSOCIATED CONTENT

Supporting Information

The Supporting Information is available free of charge on the ACS Publications website at DOI: 10.1021/acsami.7b09743.

Materials and methods describing PDMS spin coating, PDMS thickness measurements, and FRAP measurements. Data and figures of PDMS stamps, thickness of PDS coverslips, micropatterns on PDMS-coated coverslips, FRAP diffusion, and localization accuracy (PDF)

Videos of actin distribution in rectangular-patterned cells, of sptPALM, and of dSTORM imaging on HMDS versus PDMS substrates (MOV)(MOV)(MOV)

■ AUTHOR INFORMATION

Corresponding Author

*E-mail: pinaud@usc.edu.

ORCID

Fabien Pinaud: 0000-0002-4272-3616

Author Contributions

A.F., M.B., R.S., and T.C. designed and performed experiments and contributed reagents and analyses. F.P. conceived and supervised the research, designed experiments, and contributed analyses. A.F. and F.P. wrote the manuscript.

Notes

The authors declare no competing financial interest.

■ ACKNOWLEDGMENTS

This work was supported in part by the National Science Foundation, Division of Material Research, under Grant No. 1406812. We would like to thank Matthew Michael for access to his confocal microscope, Jongseung Yoon for assistance in PDMS stamp fabrication, and Juliet Ellis for kindly providing cDNA encoding emerin.

■ REFERENCES

(1) Kumar, A.; Biebuyck, H. A.; Whitesides, G. M. Patterning Self-Assembled Monolayers: Applications in Materials Science. *Langmuir* **1994**, *10*, 1498−1511.

DOI: 10.1021/acsami.7b09743
ACS Appl. Mater. Interfaces XXXX, XXX, XXX−XXX

(2) D'Arcangelo, E.; McGuigan, A. P. Micropatterning Strategies to Engineer Controlled Cell and Tissue Architecture in Vitro. *Biotechniques* **2015**, *58*, 13−23.
(3) Petrak, D.; Atefi, E.; Yin, L.; Chilian, W.; Tavana, H. Automated, Spatio-Temporally Controlled Cell Microprinting with Polymeric Aqueous Biphasic System. *Biotechnol. Bioeng.* **2014**, *111*, 404−412.
(4) Revzin, A.; Rajagopalan, P.; Tilles, A. W.; Berthiaume, F.; Yarmush, M. L.; Toner, M. Designing a Hepatocellular Microenvironment with Protein Microarraying and Poly(Ethylene Glycol) Photolithography. *Langmuir* **2004**, *20*, 2999−3005.
(5) Suh, K. Y.; Seong, J.; Khademhosseini, A.; Laibinis, P. E.; Langer, R. A Simple Soft Lithographic Route to Fabrication of Poly(Ethylene Glycol) Microstructures for Protein and Cell Patterning. *Biomaterials* **2004**, *25*, 557−563.
(6) Folch, A.; Jo, B. H.; Hurtado, O.; Beebe, D. J.; Toner, M. Microfabricated Elastomeric Stencils for Micropatterning Cell Cultures. *J. Biomed. Mater. Res.* **2000**, *52*, 346−353.
(7) Nie, Z.; Kumacheva, E. Patterning Surfaces with Functional Polymers. *Nat. Mater.* **2008**, *7*, 277−290.
(8) Azioune, A.; Storch, M.; Bornens, M.; Thery, M.; Piel, M. Simple and Rapid Process for Single Cell Micro-Patterning. *Lab Chip* **2009**, *9*, 1640−1642.
(9) Chen, C. S.; Mrksich, M.; Huang, S.; Whitesides, G. M.; Ingber, D. E. Geometric Control of Cell Life and Death. *Science* **1997**, *276*, 1425−1428.
(10) Azioune, A.; Carpi, N.; Tseng, Q.; Thery, M.; Piel, M. Protein Micropatterns: A Direct Printing Protocol Using Deep UVs. *Methods Cell Biol.* **2010**, *97*, 133−146.
(11) Labouesse, C.; Verkhovsky, A. B.; Meister, J. J.; Gabella, C.; Vianay, B. Cell Shape Dynamics Reveal Balance of Elasticity and Contractility in Peripheral Arcs. *Biophys. J.* **2015**, *108*, 2437−2447.
(12) Bischofs, I. B.; Klein, F.; Lehnert, D.; Bastmeyer, M.; Schwarz, U. S. Filamentous Network Mechanics and Active Contractility Determine Cell and Tissue Shape. *Biophys. J.* **2008**, *95*, 3488−3496.
(13) Rigato, A.; Rico, F.; Eghiaian, F.; Piel, M.; Scheuring, S. Atomic Force Microscopy Mechanical Mapping of Micropatterned Cells Shows Adhesion Geometry-Dependent Mechanical Response on Local and Global Scales. *ACS Nano* **2015**, *9*, 5846−5856.
(14) Fu, J.; Wang, Y. K.; Yang, M. T.; Desai, R. A.; Yu, X.; Liu, Z.; Chen, C. S. Mechanical Regulation of Cell Function with Geometrically Modulated Elastomeric Substrates. *Nat. Methods* **2010**, *7*, 733−736.
(15) Tan, X.; Heureaux, J.; Liu, A. P. Cell Spreading Area Regulates Clathrin-Coated Pit Dynamics on Micropatterned Substrate. *Integr. Biol.* **2015**, *7*, 1033−1043.
(16) Versaevel, M.; Grevesse, T.; Gabriele, S. Spatial Coordination between Cell and Nuclear Shape within Micropatterned Endothelial Cells. *Nat. Commun.* **2012**, *3*, No. 671.
(17) Khatau, S. B.; Hale, C. M.; Stewart-Hutchinson, P. J.; Patel, M. S.; Stewart, C. L.; Searson, P. C.; Hodzic, D.; Wirtz, D. A Perinuclear Actin Cap Regulates Nuclear Shape. *Proc. Natl. Acad. Sci. U.S.A.* **2009**, *106*, 19017−19022.
(18) Wegel, E.; Gohler, A.; Lagerholm, B. C.; Wainman, A.; Uphoff, S.; Kaufmann, R.; Dobbie, I. M. Imaging Cellular Structures in Super-Resolution with Sim, Sted and Localisation Microscopy: A Practical Comparison. *Sci. Rep.* **2016**, *6*, No. 27290.
(19) Versaevel, M.; Braquenier, J. B.; Riaz, M.; Grevesse, T.; Lantoine, J.; Gabriele, S. Super-Resolution Microscopy Reveals Linc Complex Recruitment at Nuclear Indentation Sites. *Sci. Rep.* **2014**, *4*, No. 7362.
(20) Koschwanez, J. H.; Carlson, R. H.; Meldrum, D. R. Thin Pdms Films Using Long Spin Times or Tert-Butyl Alcohol as a Solvent. *PLoS One* **2009**, *4*, No. e4572.
(21) Gutierrez, E.; Tkachenko, E.; Besser, A.; Sundd, P.; Ley, K.; Danuser, G.; Ginsberg, M. H.; Groisman, A. High Refractive Index Silicone Gels for Simultaneous Total Internal Reflection Fluorescence and Traction Force Microscopy of Adherent Cells. *PLoS One* **2011**, *6*, No. e23807.
(22) Löchte, S.; Waichman, S.; Beutel, O.; You, C.; Piehler, J. Live Cell Micropatterning Reveals the Dynamics of Signaling Complexes at the Plasma Membrane. *J. Cell Biol.* **2014**, *207*, 407−418.
(23) Lajoie, P.; Goetz, J. G.; Dennis, J. W.; Nabi, I. R. Lattices, Rafts, and Scaffolds: Domain Regulation of Receptor Signaling at the Plasma Membrane. *J. Cell Biol.* **2009**, *185*, 381−385.
(24) Rothberg, K. G.; Heuser, J. E.; Donzell, W. C.; Ying, Y. S.; Glenney, J. R.; Anderson, R. G. Caveolin, a Protein Component of Caveolae Membrane Coats. *Cell* **1992**, *68*, 673−682.
(25) Schlörmann, W.; Steiniger, F.; Richter, W.; Kaufmann, R.; Hause, G.; Lemke, C.; Westermann, M. The Shape of Caveolae Is Omega-Like after Glutaraldehyde Fixation and Cup-Like after Cryofixation. *Histochem. Cell Biol.* **2010**, *133*, 223−228.
(26) Lebbink, M. N.; Jimenez, N.; Vocking, K.; Hekking, L. H.; Verkleij, A. J.; Post, J. A. Spiral Coating of the Endothelial Caveolar Membranes as Revealed by Electron Tomography and Template Matching. *Traffic* **2010**, *11*, 138−150.
(27) Nassoy, P.; Lamaze, C. Stressing Caveolae New Role in Cell Mechanics. *Trends Cell Biol.* **2012**, *22*, 381−389.
(28) Sinha, B.; Koster, D.; Ruez, R.; Gonnord, P.; Bastiani, M.; Abankwa, D.; Stan, R. V.; Butler-Browne, G.; Vedie, B.; Johannes, L.; Morone, N.; Parton, R. G.; Raposo, G.; Sens, P.; Lamaze, C.; Nassoy, P. Cells Respond to Mechanical Stress by Rapid Disassembly of Caveolae. *Cell* **2011**, *144*, 402−413.
(29) Echarri, A.; Del Pozo, M. A. Caveolae - Mechanosensitive Membrane Invaginations Linked to Actin Filaments. *J. Cell Sci.* **2015**, *128*, 2747−2758.
(30) Joshi, B.; Strugnell, S. S.; Goetz, J. G.; Kojic, L. D.; Cox, M. E.; Griffith, O. L.; Chan, S. K.; Jones, S. J.; Leung, S. P.; Masoudi, H.; Leung, S.; Wiseman, S. M.; Nabi, I. R. Phosphorylated Caveolin-1 Regulates Rho/Rock-Dependent Focal Adhesion Dynamics and Tumor Cell Migration and Invasion. *Cancer Res.* **2008**, *68*, 8210−8220.
(31) Drab, M.; Verkade, P.; Elger, M.; Kasper, M.; Lohn, M.; Lauterbach, B.; Menne, J.; Lindschau, C.; Mende, F.; Luft, F. C.; Schedl, A.; Haller, H.; Kurzchalia, T. V. Loss of Caveolae, Vascular Dysfunction, and Pulmonary Defects in Caveolin-1 Gene-Disrupted Mice. *Science* **2001**, *293*, 2449−2452.
(32) Razani, B.; Engelman, J. A.; Wang, X. B.; Schubert, W.; Zhang, X. L.; Marks, C. B.; Macaluso, F.; Russell, R. G.; Li, M.; Pestell, R. G.; Di Vizio, D.; Hou, H., Jr.; Kneitz, B.; Lagaud, G.; Christ, G. J.; Edelmann, W.; Lisanti, M. P. Caveolin-1 Null Mice Are Viable but Show Evidence of Hyperproliferative and Vascular Abnormalities. *J. Biol. Chem.* **2001**, *276*, 38121−38138.
(33) Ostlund, C.; Ellenberg, J.; Hallberg, E.; Lippincott-Schwartz, J.; Worman, H. J. Intracellular Trafficking of Emerin, the Emery-Dreifuss Muscular Dystrophy Protein. *J. Cell Sci.* **1999**, *112*, 1709−1719.
(34) Manilal, S.; Nguyen, T. M.; Sewry, C. A.; Morris, G. E. The Emery-Dreifuss Muscular Dystrophy Protein, Emerin, Is a Nuclear Membrane Protein. *Hum. Mol. Genet.* **1996**, *5*, 801−808.
(35) Berk, J. M.; Tifft, K. E.; Wilson, K. L. The Nuclear Envelope Lem-Domain Protein Emerin. *Nucleus* **2013**, *4*, 298−314.
(36) Holmer, L.; Worman, H. J. Inner Nuclear Membrane Proteins: Functions and Targeting. *Cell. Mol. Life Sci.* **2001**, *58*, 1741−1747.
(37) Ho, C. Y.; Jaalouk, D. E.; Vartiainen, M. K.; Lammerding, J. Lamin a/C and Emerin Regulate Mkl1-Srf Activity by Modulating Actin Dynamics. *Nature* **2013**, *497*, 507−511.
(38) Chang, W.; Folker, E. S.; Worman, H. J.; Gundersen, G. G. Emerin Organizes Actin Flow for Nuclear Movement and Centrosome Orientation in Migrating Fibroblasts. *Mol. Biol. Cell* **2013**, *24*, 3869−3680.
(39) Guilluy, C.; Osborne, L. D.; Van Landeghem, L.; Sharek, L.; Superfine, R.; Garcia-Mata, R.; Burridge, K. Isolated Nuclei Adapt to Force and Reveal a Mechanotransduction Pathway in the Nucleus. *Nat. Cell Biol.* **2014**, *16*, 376−381.
(40) Wang, N.; Tytell, J. D.; Ingber, D. E. Mechanotransduction at a Distance: Mechanically Coupling the Extracellular Matrix with the Nucleus. *Nat. Rev. Mol. Cell Biol.* **2009**, *10*, 75−82.
(41) Lammerding, J.; Hsiao, J.; Schulze, P. C.; Kozlov, S.; Stewart, C. L.; Lee, R. T. Abnormal Nuclear Shape and Impaired Mechano-

DOI: 10.1021/acsami.7b09743
ACS Appl. Mater. Interfaces XXXX, XXX, XXX−XXX

transduction in Emerin-Deficient Cells. *J. Cell Biol.* **2005**, *170*, 781−791.
(42) Capell, B. C.; Collins, F. S. Human Laminopathies: Nuclei Gone Genetically Awry. *Nat. Rev. Genet.* **2006**, *7*, 940−952.
(43) Mujawar, L. H.; Norde, W.; van Amerongen, A. Spot Morphology of Non-Contact Printed Protein Molecules on Non-Porous Substrates with a Range of Hydrophobicities. *Analyst* **2013**, *138*, 518−524.
(44) Li, Q.; Kumar, A.; Makhija, E.; Shivashankar, G. V. The Regulation of Dynamic Mechanical Coupling between Actin Cytoskeleton and Nucleus by Matrix Geometry. *Biomaterials* **2014**, *35*, 961−969.
(45) Manley, S.; Gillette, J. M.; Patterson, G. H.; Shroff, H.; Hess, H. F.; Betzig, E.; Lippincott-Schwartz, J. High-Density Mapping of Single-Molecule Trajectories with Photoactivated Localization Microscopy. *Nat. Methods* **2008**, *5*, 155−157.
(46) Tokunaga, M.; Imamoto, N.; Sakata-Sogawa, K. Highly Inclined Thin Illumination Enables Clear Single-Molecule Imaging in Cells. *Nat. Methods* **2008**, *5*, 159−161.
(47) Shimi, T.; Koujin, T.; Segura-Totten, M.; Wilson, K. L.; Haraguchi, T.; Hiraoka, Y. Dynamic Interaction between Baf and Emerin Revealed by Frap, Flip, and Fret Analyses in Living Hela Cells. *J. Struct. Biol.* **2004**, *147*, 31−41.
(48) Schütz, G. J.; Schindler, H.; Schmidt, T. Single-Molecule Microscopy on Model Membranes Reveals Anomalous Diffusion. *Biophys. J.* **1997**, *73*, 1073−1080.
(49) Rowat, A. C.; Lammerding, J.; Ipsen, J. H. Mechanical Properties of the Cell Nucleus and the Effect of Emerin Deficiency. *Biophys. J.* **2006**, *91*, 4649−4664.
(50) Osmanagic-Myers, S.; Dechat, T.; Foisner, R. Lamins at the Crossroads of Mechanosignaling. *Genes Dev.* **2015**, *29*, 225−237.
(51) Ostlund, C.; Sullivan, T.; Stewart, C. L.; Worman, H. J. Dependence of Diffusional Mobility of Integral Inner Nuclear Membrane Proteins on a-Type Lamins. *Biochemistry* **2006**, *45*, 1374−1382.
(52) Heilemann, M.; van de Linde, S.; Schuttpelz, M.; Kasper, R.; Seefeldt, B.; Mukherjee, A.; Tinnefeld, P.; Sauer, M. Subdiffraction-Resolution Fluorescence Imaging with Conventional Fluorescent Probes. *Angew. Chem., Int. Ed. Engl.* **2008**, *47*, 6172−6176.
(53) Kronstein, R.; Seebach, J.; Grossklaus, S.; Minten, C.; Engelhardt, B.; Drab, M.; Liebner, S.; Arsenijevic, Y.; Taha, A. A.; Afanasieva, T.; Schnittler, H. J. Caveolin-1 Opens Endothelial Cell Junctions by Targeting Catenins. *Cardiovasc. Res.* **2012**, *93*, 130−140.
(54) Keppler, A.; Gendreizig, S.; Gronemeyer, T.; Pick, H.; Vogel, H.; Johnsson, K. A General Method for the Covalent Labeling of Fusion Proteins with Small Molecules in Vivo. *Nat. Biotechnol.* **2003**, *21*, 86−89.
(55) Zheng, Y. Z.; Boscher, C.; Inder, K. L.; Fairbank, M.; Loo, D.; Hill, M. M.; Nabi, I. R.; Foster, L. J. Differential Impact of Caveolae and Caveolin-1 Scaffolds on the Membrane Raft Proteome. *Mol. Cell. Proteomics* **2011**, *10*, No. M110.007146.
(56) Müller, A.; Meyer, J.; Paumer, T.; Pompe, T. Cytoskeletal Transition in Patterned Cells Correlates with Interfacial Energy Model. *Soft Matter* **2014**, *10*, 2444−2452.
(57) Lo, H. P.; Hall, T. E.; Parton, R. G. Mechanoprotection by Skeletal Muscle Caveolae. *Bioarchitecture* **2016**, *6*, 22−27.
(58) Knies, Y.; Bernd, A.; Kaufmann, R.; Bereiter-Hahn, J.; Kippenberger, S. Mechanical Stretch Induces Clustering of Beta1-Integrins and Facilitates Adhesion. *Exp. Dermatol.* **2006**, *15*, 347−355.
(59) Iwamoto, D. V.; Calderwood, D. A. Regulation of Integrin-Mediated Adhesions. *Curr. Opin. Cell Biol.* **2015**, *36*, 41−47.
(60) Sergé, A.; Bertaux, N.; Rigneault, H.; Marguet, D. Dynamic Multiple-Target Tracing to Probe Spatiotemporal Cartography of Cell Membranes. *Nat. Methods* **2008**, *5*, 687−694.
(61) Thompson, R. E.; Larson, D. R.; Webb, W. W. Precise Nanometer Localization Analysis for Individual Fluorescent Probes. *Biophys. J.* **2002**, *82*, 2775−2783.
(62) Wolter, S.; Loschberger, A.; Holm, T.; Aufmkolk, S.; Dabauvalle, M. C.; van de Linde, S.; Sauer, M. Rapidstorm: Accurate, Fast Open-Source Software for Localization Microscopy. *Nat. Methods* **2012**, *9*, 1040−1041.
(63) Pengo, T.; Holden, S. J.; Manley, S. Palmsiever: A Tool to Turn Raw Data into Results for Single-Molecule Localization Microscopy. *Bioinformatics* **2015**, *31*, 797−798.
(64) Schneider, C. A.; Rasband, W. S.; Eliceiri, K. W. Nih Image to Imagej: 25 Years of Image Analysis. *Nat. Methods* **2012**, *9*, 671−675.
(65) Huang, B.; Wang, W.; Bates, M.; Zhuang, X. Three-Dimensional Super-Resolution Imaging by Stochastic Optical Reconstruction Microscopy. *Science* **2008**, *319*, 810−813.
(66) Condit, R.; Ashton, P. S.; Baker, P.; Bunyavejchewin, S.; Gunatilleke, S.; Gunatilleke, N.; Hubbell, S. P.; Foster, R. B.; Itoh, A.; LaFrankie, J. V.; Lee, H. S.; Losos, E.; Manokaran, N.; Sukumar, R.; Yamakura, T. Spatial Patterns in the Distribution of Tropical Tree Species. *Science* **2000**, *288*, 1414−1418.
(67) Perry, G. L. W. Sppack: Spatial Point Pattern Analysis in Excel Using Visual Basic for Applications (Vba). *Environ. Modell. Software* **2004**, *19*, 559−569.
(68) Haase, P. Spatial Pattern Analysis in Ecology Based on Ripley's K-Function: Introduction and Methods of Edge Correction. *J. Veg. Sci.* **1995**, *6*, 575−582.
(69) Sengupta, P.; Jovanovic-Talisman, T.; Skoko, D.; Renz, M.; Veatch, S. L.; Lippincott-Schwartz, J. Probing Protein Heterogeneity in the Plasma Membrane Using Palm and Pair Correlation Analysis. *Nat. Methods* **2011**, *8*, 969−975.
(70) Veatch, S. L.; Machta, B. B.; Shelby, S. A.; Chiang, E. N.; Holowka, D. A.; Baird, B. A. Correlation Functions Quantify Super-Resolution Images and Estimate Apparent Clustering Due to over-Counting. *PLoS One* **2012**, *7*, No. e31457.

DOI: 10.1021/acsami.7b09743
ACS Appl. Mater. Interfaces XXXX, XXX, XXX−XXX